Energy Engineering

Tech Science Press

Doi:10.32604/ee.2025.070750

ARTICLE

Numerical Simulation of Cross-Layer Propagation Mechanisms for Hydraulic Fractures in Deep Coal-Rock Formations

Zhirong Jin[1,*], Xiaorui Hou[1], Yanrong Ge[1], Tiankui Guo[2], Ming Chen[2], Shuyi Li[2] and Tianyu Niu[2]

[1]Research Institute of Petroleum Engineering Technology, SINOPEC Jiangsu Oilfield Company, Yangzhou, 225009, China
[2]School of Petroleum Engineering, China University of Petroleum (East China), Qingdao, 266580, China

*Corresponding Author: Zhirong Jin. Email: jinzr.jsyt@sinopec.com

Received: 23 July 2025; Accepted: 12 September 2025; Published: 27 January 2026

ABSTRACT: Hydraulic fracturing serves as a critical technology for reservoir stimulation in deep coalbed methane (CBM) development, where the mechanical properties of gangue layers exert a significant control on fracture propagation behavior. To address the unclear mechanisms governing fracture penetration across coal-gangue interfaces, this study employs the Continuum-Discontinuum Element Method (CDEM) to simulate and analyze the vertical propagation of hydraulic fractures initiating within coal seams, based on geomechanical parameters derived from the deep Benxi Formation coal seams in the southeastern Ordos Basin. The investigation systematically examines the influence of geological and operational parameters on cross-interfacial fracture growth. Results demonstrate that vertical stress difference, elastic modulus contrast between coal and gangue layers, interfacial stress differential, and interfacial cohesion at coal-gangue interfaces are critical factors governing hydraulic fracture penetration through these interfaces. High vertical stress differences (>3 MPa) inhibit interfacial dilation, promoting predominant cross-layer fracture propagation. Reduced interfacial stress contrasts and enhanced interfacial cohesion facilitate fracture penetration across interfaces. Furthermore, smaller elastic modulus contrasts between coal and gangue correlate with increased interfacial aperture. Finally, lower injection rates effectively suppress vertical fracture propagation in deep coal reservoirs. This study elucidates the characteristics and mechanisms governing cross-layer fracture propagation in coal–rock composites with interbedded partings, and delineates the dynamic evolution laws and dominant controlling factors involved. The findings provide critical theoretical insights for the optimization of fracture design and the efficient development of deep coalbed methane reservoirs.

KEYWORDS: Deep coal-rock formations; cross-layer fracturing; fluid-solid coupling; fracture propagation behavior; numerical simulation

1 Introduction

China possesses abundant coalbed methane (CBM) resources. According to the national CBM resource assessment prediction, the total geological resources of CBM stored in different regions and at varying depths are approximately 80×10^{12} m^3. Among these, deep coalbed methane (at depths exceeding 2000 m) accounts for about 40.47×10^{12} m^3, representing over half of the total resources and indicating vast development potential [1–4]. However, compared to mid-shallow coal reservoirs, deep coal-rock formations exhibit distinct characteristics including high *in-situ* stress, low permeability, well-developed natural weaknesses (such as bedding planes and cleats), and strong heterogeneity. These properties result in rapid production decline in single wells and poor economic returns [5,6]. In this context, hydraulic fracturing serves as a key enabler for unlocking deep coalbed methane resources, with its core objective being to interconnect

Copyright © 2026 The Authors. Published by Tech Science Press.
This work is licensed under a Creative Commons Attribution 4.0 International License, which permits unrestricted use, distribution, and reproduction in any medium, provided the original work is properly cited.

natural fractures within coal reservoirs via engineered fractures, thereby establishing high-conductivity flow pathways that facilitate dewatering-induced gas recovery through reservoir pressure depletion, ultimately enhancing gas desorption kinetics and production capacity [7–9].

The widely developed gangue layers in the deep coal seams of the Benxi Formation, southeastern Ordos Basin, display a vertically stacked and laterally discontinuous spatial pattern. Composed mainly of carbonaceous mudstone, siltstone, and thin limestone interbeds, these layers possess distinct rock mechanical properties, stress conditions, and permeability compared to the coal seams. These differences play a key role in controlling the vertical growth of hydraulic fractures. Therefore, effective containment of fracture height is crucial for successful coalbed methane (CBM) production in such reservoirs [10–12]. Regarding hydraulic fracture vertical propagation, domestic and international researchers have conducted extensive studies through physical experiments and numerical simulations. Daneshy et al. [13] performed hydraulic fracture interlayer propagation experiments using sandstone-limestone composite specimens, revealing that higher interfacial cementation strength facilitates fracture penetration across layer interfaces. Zhao and Chen [14] established a critical criterion for hydraulic fracture propagation behavior at interlayer interfaces based on rock fracture mechanics theory, mechanically explaining the causes of interfacial slippage. Tan Peng et al. [15] conducted true triaxial hydraulic fracturing physical simulation tests to investigate parameters such as *in-situ* stress contrast, elastic modulus contrast, and coal cleat systems on fracture propagation across coal-sandstone interfaces. Tian et al. [16] employed ABAQUS software to establish a two-dimensional fluid-solid coupling finite element model incorporating natural cleat networks and globally embedded cohesive zone models (CZM). This model simulated the effects of cleat orientation, cleat density, coal-mudstone length ratio, and injection rate on hydraulic fracture propagation behavior. Ren et al. [17] and Xu et al. [18] utilized numerical simulation methods to study the influence of fracturing fluid injection rate and viscosity on vertical fracture propagation. Their results demonstrated that higher injection rates and viscosities significantly promote vertical fracture extension. Huang et al. [19] combined true triaxial hydraulic fracturing experiments with numerical simulations to investigate the impact of coal bedding planes on hydraulic fracture propagation. Their findings indicated that the dip angle of coal bedding planes exerts a more significant influence on fracture propagation than the maximum principal stress, while optimized injection rates facilitate the formation of complex hydraulic fracture networks. Current research on hydraulic fracture penetration in coal formations primarily focuses on single coal seams and shallow to medium-depth sand-coal composite interfaces. These studies exhibit limitations in characterizing the complex interfacial mechanical behavior and stress response characteristics of deep multilayered formations. Furthermore, there is scarce reported research on the influence of bedding planes at deep coal-gangue interfaces on the laws governing hydraulic fracture penetration.

Based on previous research, this study employs mechanical parameters derived from deep coal seams in the Benxi Formation along the southeastern margin of the Ordos Basin. A two-dimensional numerical model for the vertical propagation of hydraulic fractures at deep coal-interlayer interfaces was constructed using the Continuum-Discontinuum Element Method (CDEM). Following model validation, the influence of geological parameters (*in-situ* stress, interlayer stress, cohesion, and Young's modulus) and engineering parameters (fracturing fluid injection rate) on cross-layer fracture propagation was systematically investigated. Through this study, the influence of deep coal gangue layer and weak bedding structure on the longitudinal propagation of cracks is systematically revealed, which can provide a theoretical basis for the optimal control of fracture height in the field fracturing process, so as to promote the effective formation of complex fracture network in coal and rock strata.

2 Numerical Methods and Constitutive Models

2.1 Continuum-Discontinuum Element Method

In CDEM numerical simulations, the computational framework is composed of two primary components: blocks and interfaces (Fig. 1). Blocks, which may consist of one or multiple finite elements, are used to represent the continuous behavior of materials. An interface is defined as the common boundary between two adjacent blocks and captures discontinuous material behavior. Interfaces in CDEM include both real and virtual types. Real interfaces occur at physical contacts between blocks, while virtual interfaces arise from the discretization boundaries between finite elements within a single block. Although virtual interfaces share the same constitutive models as real interfaces, they differ in their parameter assignments. Finite elements within blocks are interconnected by springs located at shared nodes. When a spring element meets predefined fracture criteria, its rupture dynamically propagates alterations in contact forces and displacements. This method allows for accurate simulation of crack propagation in materials.

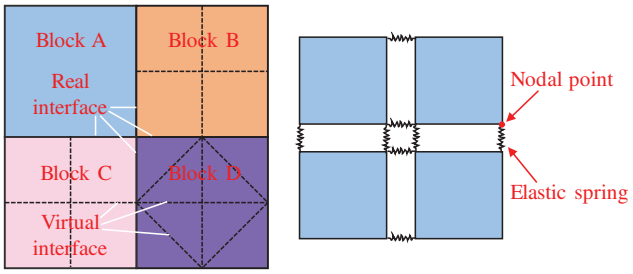

Figure 1: Schematic diagram of CDEM numerical model

The core governing particle motion equation in CDEM is [20]:

$$\boldsymbol{M}\boldsymbol{a}_n + \boldsymbol{C}\boldsymbol{v}_n + \boldsymbol{I}\boldsymbol{u}_n = \boldsymbol{F} + \boldsymbol{F}_{\mathrm{bd}} + \boldsymbol{F}_{\mathrm{bc}} + \boldsymbol{F}_{\mathrm{jd}} + \boldsymbol{F}_{\mathrm{jc}} \tag{1}$$

where $\boldsymbol{a}_n$ denotes the nodal acceleration column vector. $\boldsymbol{v}_n$ the nodal velocity column vector, and $\boldsymbol{u}_n$ the nodal displacement column vector. $\boldsymbol{M}$ represents the element mass matrix. $\boldsymbol{C}$ the element damping matrix, and $\boldsymbol{I}$ the element stiffness matrix. $\boldsymbol{F}$ is the external force column vector acting on nodes. $\boldsymbol{F}_{\mathrm{bd}}$, $\boldsymbol{F}_{\mathrm{bc}}$, $\boldsymbol{F}_{\mathrm{jd}}$, $\boldsymbol{F}_{\mathrm{jc}}$ respectively denote the block deformation force column vector, block contact damping force column vector, interface deformation force column vector, and interface contact damping force column vector.

The governing equation for nodal motion calculation is:

$$\begin{cases} v = \sum_{t=0}^{T_{now}} a\Delta t & a = \frac{F}{m} \\ u = \sum_{t=0}^{T_{now}} \Delta u & \Delta u = v\Delta t \end{cases} \tag{2}$$

where a represents nodal acceleration. $v$denotes nodal velocity. u indicates total nodal displacement, and Δu signifies incremental nodal displacement. m stands for nodal mass, and Δt is the computational time step. By iteratively solving Eqs. (1) and (2), an explicit solution procedure is achieved.

2.2 Hydro-Mechanical Coupled Fracture Propagation Computational Model

CDEM is a numerical methodology grounded in the Generalized Lagrangian Formulation. It facilitates accurate simulation of dynamic stress evolution in continuous media and captures discontinuous mechanical

behaviors during fracture propagation through a coupled finite-discrete element framework. By incorporating a fluid flow model into the solid mechanical formulation, an elastic-damage-fracture constitutive model for hydraulic fracture propagation is established within the CDEM framework [21]. The porous flow computation employs the same nodal discretization as the solid domain. Fracture elements are incorporated at interfaces where discontinuities exist. The stress field in the continuum region is resolved through solid finite element analysis, while fracture networks are represented by establishing fluid conduits along fracture elements located at the contact surfaces between solid elements. This coupled formulation enables complete modeling of fluid flow within both existing joints and actively propagating fractures.

2.2.1 Elastic-Damage-Fracture Constitutive Model

This research employs an elastic-damage-fracture constitutive model to simulate the mechanical behavior of rock masses. Within this framework, a linear elastic constitutive relationship is applied to each finite element. The input parameters for the linear elastic model include the elastic modulus, Poisson's ratio, tensile strength, and internal friction angle. At the virtual interfaces, a damage-fracture constitutive model is utilized. The input parameters for this interfacial model comprise the contact normal stiffness, contact tangential stiffness, internal friction angle, tensile strength, tensile fracture energy, and shear fracture energy.

The incremental formulation of the linear elastic constitutive relationship for elements is expressed as [22]:

$$\Delta\sigma_{ij} = 2G\Delta\varepsilon_{ij} + \left(K - \frac{2}{3}G\right)\Delta\theta\delta_{ij} \tag{3}$$

$$\sigma_{ij}\left(\lambda_1\right) = \Delta\sigma_{ij} + \sigma_{ij}\left(\lambda_0\right) \tag{4}$$

where σ_{ij} denotes the stress tensor, Pa. $\Delta\sigma_{ij}$ represents the incremental stress tensor, Pa. $\Delta\varepsilon_{ij}$ is the incremental strain tensor, and $\Delta\theta$ signifies the incremental volumetric strain. K indicates the bulk modulus, Pa. G is the shear modulus, Pa and δ_{ij} denotes the Kronecker delta. The subscript λ_1 refers to the next time step, while λ_0 corresponds to the current time step.

At virtual interfaces, a maximum tensile stress criterion with linear strength-softening and a Mohr–Coulomb model are employed to represent the damage and fracture behavior. The corresponding normal and tangential contact forces at these interfaces are then resolved for the next time step using an incremental formulation [23].

$$\begin{cases} F_n\left(\lambda_1\right) = F_n\left(\lambda_0\right) - k_n A_c \Delta du_n \\ F_s\left(\lambda_1\right) = F_s\left(\lambda_0\right) - k_s A_c \Delta du_s \end{cases} \tag{5}$$

where F_n and F_s denote the normal and tangential contact forces, N. k_n and k_s represent the normal and tangential contact stiffness per unit area, Pa·m^{-1}. A_c indicates the virtual interface area, m^2 and Δdu_n and Δdu_s signify the increments of normal and tangential relative displacement, m.

The occurrence of tensile failure is assessed based on whether the following condition is satisfied:

$$-F_n\left(\lambda_1\right) \geq \sigma_t\left(\lambda_0\right) A_c \tag{6}$$

Then tensile failure is identified, requiring recalibration of the normal contact force and tensile resistance:

$$F_n\left(\lambda_1\right) = -\sigma_t\left(\lambda_0\right) A_c \tag{7}$$

$$\sigma_t(\lambda_1) = -(\sigma_{t0})^2 \Delta u_n / \left(2G_{ft}\right) + \sigma_t \tag{8}$$

where σ_{t0} represents the initial tensile strength at the virtual interface, Pa. $\sigma_t(\lambda_0)$ and $\sigma_t(\lambda_1)$ denote the tensile strength at the current time step and next time step, Pa. Δu_n indicates the normal relative displacement at the current time step, m. G_{ft} signifies the tensile fracture energy, Pa·m.

The determination of shear failure occurrence is conducted using Eq. (9), if:

$$-F_s(\lambda_1) \geq F_n(\lambda_1) \tan\phi + c(\lambda_0) A_c \tag{9}$$

Upon occurrence of shear failure in the spring, the tangential contact force and cohesive force require revision to the following:

$$\begin{cases} F_s(\lambda_1) = F_n(\lambda_1) \tan\phi + c(\lambda_0) A_c \\ c(\lambda_1) = -(c_0)^2 \Delta u_s / \left(2G_{fs}\right) + c_0 \end{cases} \tag{10}$$

where ϕ denotes the internal friction angle at the virtual interface, °. c_0, $c(\lambda_0)$ and $c(\lambda_1)$ represent the cohesion at the initial time step, current time step, and next time step, Pa. Δu_s indicates the tangential relative displacement at the current time step, m. and G_{fs} signifies the shear fracture energy, Pa·m.

Based on Eqs. (6)–(10), the constitutive curves for normal and tangential directions at virtual interfaces can be plotted, as illustrated in Fig. 2.

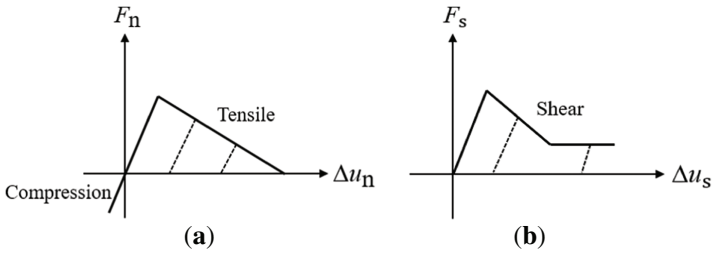

Figure 2: Constitutive curves at virtual interfaces. (**a**) Normal constitutive curves; (**b**) Tangential constitutive curves

2.2.2 The Principle of Seepage-Stress Coupling in Fracture Networks

During hydraulic fracturing, fracture seepage is modeled using finite element-based seepage networks coupled with solid mechanical formulations. The interaction between the stress field and the seepage field is facilitated by the coupling of virtual interfaces with the fracture flow pathways [24]. Specifically, fracture seepage applies fluid pressure onto the virtual interfaces, while the deformation of the surrounding rock—induced through these interfaces—regulates fracture apertures, thereby governing the subsequent seepage behavior.

Fluid flow through fractures adheres to Darcy's law:

$$v = -\frac{k}{\mu} \nabla P = -\frac{k}{\mu} \frac{\partial P}{\partial x_i} \tag{11}$$

where v represents the flow velocity of fracture seepage, m/s. k denotes the permeability of the fracture, m^2. μ indicates fluid dynamic viscosity, Pa·s. P signifies the fluid pressure within the fracture, Pa. and x_i corresponds to the coordinate component of node i in a given direction within the element, m.

Cubic Law states that the fluid flow rate per unit width through a fracture is proportional to the cube of the fracture aperture [25]. The proportionality constant depends on the fluid viscosity and the pressure gradient acting across the fracture:

$$q = \frac{gb^3}{12\vartheta}J \tag{12}$$

where q represents the seepage flow rate per unit width, m^2/s. g denotes the gravitational acceleration, m/s^2. b is the fracture aperture, m. ϑ indicates the kinematic viscosity of the fluid flow, $\vartheta = \rho\upsilon$, m^2/s; and J signifies the hydraulic gradient, dimensionless.

The total flow rate of fluid passing through the fracture can be calculated based on the product of the seepage flow rate per unit width and the fracture spacing:

$$Q = \frac{gwb^3}{12\vartheta}J \tag{13}$$

where Q represents the flow rate through the fracture, m^3/s. and w denotes the fracture spacing, m.

According to Cubic Law, for single-phase Newtonian fluid undergoing laminar flow within a fracture, the volumetric flow rate per unit time is expressed as follows:

$$Q = k\frac{\Delta PA}{\mu L} \tag{14}$$

where A represents the cross-sectional area through the fracture, $A = we$, m^2. ΔP is the pressure difference, Pa. and L denotes the fracture length, m.

Based on Eqs. (13) and (14), the permeability can be expressed as:

$$K = \frac{b^2}{12} \tag{15}$$

The seepage velocity within the fracture can be represented by:

$$v_i = kk_s\frac{\partial P}{\partial x_i} \tag{16}$$

where k denotes the fracture permeability coefficient, $m^2/(Pa{\cdot}s)$. k_s indicates the relative permeability coefficient. P represents the fluid pressure within the fracture, Pa. and x_i corresponds to the coordinate component in the direction of node i within the element, m.

When saturation equals 1, the fracture permeability coefficient can be calculated using Eqs. (11) and (16), expressed as:

$$k = \frac{K}{\mu} = \frac{b^2}{12\mu} \tag{17}$$

As illustrated in Fig. 3, when solving fracture flow fields using the Finite Volume Method (FVM), fluid pressure and saturation are stored at the grid nodes of computational cells, while fluid velocity is defined at cell centroids [26].

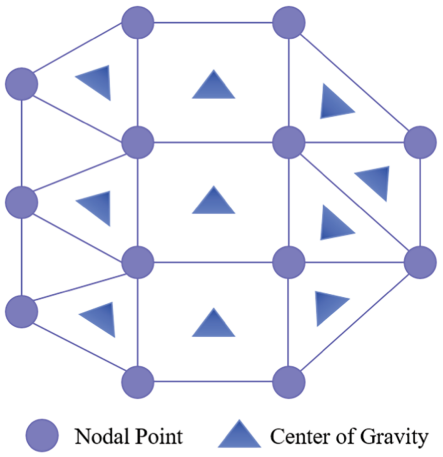

Figure 3: Schematic diagram of planar fracture element

According to the divergence theorem, the mathematical expression for nodal seepage velocity is formulated as:

$$v_i = kk_s \frac{1}{V} \sum_{j=1}^{M} \overline{P}_j n_i \Delta S_j \tag{18}$$

where V denotes the pore unit volume, m^3. M represents the total number of faces in the pore unit, dimensionless. n_i indicates the component of the unit normal vector of the j-th face associated with the current node in the i-direction. $\overline{P}_j$ signifies the average total pressure at all nodes on the j-th face of the pore unit, Pa. and ΔS_j designates the area of the j-th face, m^2.

The nodal flow rate is derived from the above as:

$$q_i = \frac{\sum_{j=1}^{M} \left(v_i \cdot n_j\right) \Delta S_j}{N_j} \tag{19}$$

where q_i is the nodal flow rate, m^3/s. v_i denotes the velocity vector of unit i, m/s. n_j is the unit outward normal vector of the j-th face of the pore unit. and N_j stands for the total number of nodes on the j-th face of the pore unit.

Based on seepage theory and mass conservation at nodes, the total seepage flow rate at a node is expressed as:

$$Q = \sum_{j=1}^{N_e} q_j \tag{20}$$

The nodal saturation is computed from the nodal flow rate in Eq. (20):

$$s = -\sum_{t=0}^{t} \left(\frac{Q + Q_{app}}{V_n} \Delta t \right) \tag{21}$$

When the fluid saturation at a computational node reaches unity (indicating fully saturated conditions), the seepage pressure at that node can be determined by solving the nodal flow Eq. (20) and saturation Eq. (21) simultaneously.

$$P_p = -\sum_{t=0}^{t} \left(k_f \frac{Q + Q_{app}}{V_n} \Delta t \right) \tag{22}$$

The total nodal pressure is then defined as:

$$P = P_p - s\rho_f \left(xg_x + yg_y + zg_z\right) \tag{23}$$

where ρ_f indicates the fluid density, kg/m^3. g_x, g_y, g_z represent the components of the global gravitational acceleration vector, m/s^2. and x, y, z are the global coordinate components of a node in the unit, m.

In the coupled analysis of the fracture seepage field and the solid stress field, fluid pressure within the fracture is applied as boundary conditions along the interface between adjacent solid elements. Conversely, the aperture along this shared boundary is computed to determine both the fracture opening and the permeability coefficient, which subsequently updates the properties of the corresponding fracture seepage elements. As illustrated in Fig. 4, edge r and edge d of solid element α are adjacent to edge m and edge h of solid element β, with fracture elements q and f sandwiched in between.

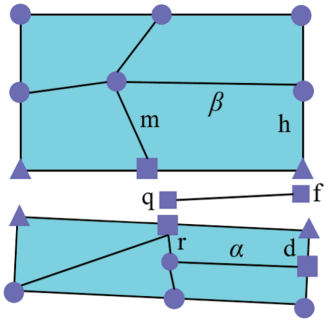

Figure 4: Schematic diagram of coupling between solid elements and fracture elements

The nodal pressures exerted by fracture elements on the four nodes (m, h, r, d) of the solid element can be expressed as:

$$\begin{cases} F_{mq} = A_m P_q \\ F_{hf} = A_h P_f \\ F_{rq} = A_r P_q \\ F_{df} = A_d P_f \end{cases} \tag{24}$$

where F_{mq}, F_{hf}, F_{rq}, F_{df} represent the nodal pressures at the four nodes, N. A_h, A_m, A_r, A_d denote the nodal areas, m^2. P_q and P_f are the nodal pressures at nodes q and f of the fracture element, Pa.

When solid boundary displacement changes, the aperture of the fracture element will be significantly affected. This relationship can be quantitatively described as:

$$\begin{cases} b_q = b_{q0} + (u_m - u_r) \\ b_f = b_{f0} + (u_h - u_d) \end{cases} \tag{25}$$

where u_h, u_m, u_r, u_d represent the displacements of the four nodes along the fracture normal direction, m. b_{q0}, b_{f0} are the initial apertures at nodes q and f of the fracture element, m.

2.2.3 Crack Propagation Criterion

In CDEM, adjacent blocks are linked by spring elements that transfer contact forces. The mechanical interactions at each contact are resolved into normal and tangential components. According to Hooke's

Law [27], the relative displacement between nodes at both ends of a contact spring is linearly related to the contact stress. Therefore, the incremental method is used to express the normal and tangential relative displacements at the next time step:

$$\begin{cases} \Delta u_{\mathrm{n}} = \dfrac{F_n}{K_{\mathrm{n}}} = \dfrac{(\sigma_{n1} + \sigma_{n2})\, A}{2K_{\mathrm{n}}} \\ \Delta u_{\mathrm{t}} = \dfrac{F_t}{K_{\mathrm{t}}} = \dfrac{(\sigma_{t1} + \sigma_{t2})\, A}{2K_{\mathrm{t}}} \end{cases} \tag{26}$$

where Δu_n and Δu_{t} are the normal and tangential relative displacements at the contact spring nodes, m. F_{n} and F_{t} are the normal and tangential contact forces at the spring ends, N. K_{n} and K_{t} are the normal and tangential stiffnesses of the contact spring, N/m. σ_{n1} and σ_{n2} are the normal stresses at two adjacent contact points, Pa. σ_{t1} and σ_{t2} are the tangential stresses at two adjacent contact points, Pa. A is the representative area of the contact point, m^2.

Hydraulic fracture initiation is characterized by the transition from continuous element boundaries to discontinuous fracture surfaces. The failure is governed by either the maximum tensile stress criterion or the Mohr–Coulomb criterion. The rupture criterion requires evaluation of three stress components: the stresses on both sides of the element, the normal stress acting on the element boundary, and the tangential stress along it. If any stress component reaches the critical failure threshold defined by Eqs. (27) or (28), the material element is judged to undergo fracture failure, and a corresponding hydraulic fracture is simulated:

$$\sigma_n \geq T \tag{27}$$

$$\sigma_t \geq c + \sigma_n \tan \varnothing \tag{28}$$

where σ_n is the normal stress, Pa. T is the tensile strength of coal rock, Pa. σ_t is the tangential stress, Pa. c is the cohesion, Pa. $\varnothing$ is the internal friction angle of the virtual interface, °.

If the spring satisfies the maximum tensile stress criterion in Eq. (27), the spring undergoes tensile fracture, and the spring force must be corrected as:

$$F_n = 0 \tag{29}$$

If the spring satisfies the Mohr-Coulomb shear failure criterion in Eq. (28), the spring undergoes shear failure, and the spring force must be modified as:

$$F_t = F_n \tan \varnothing \tag{30}$$

After spring element fracture occurs, the fracture aperture can be calculated from the displacement difference between the two nodes connected by the spring:

$$b = \left| \ (\boldsymbol{u}_1 - \boldsymbol{u}_2) \cdot \boldsymbol{n}_{12} \ \right| \tag{31}$$

where $\boldsymbol{u}_1$ and $\boldsymbol{u}_2$ are the displacements of the two nodes connected by the spring, m. $\boldsymbol{n}_{12}$ is the unit normal vector on the contact surface.

2.3 Computational Model for Hydraulic Fracture Propagation in Deep Coal Rock

2.3.1 Two-Dimensional Numerical Simulation Model for Fracture Height Propagation Considering Bedding Planes

Based on the GDEM software platform, this study utilizes its integrated CDEM method to construct a numerical model for hydraulic fracturing in deep coal rock, simulating the cross-layer propagation process of hydraulic fractures at the coal rock-parting interface. Tecplot 360 is employed as the post-processing software.

To investigate the influence of bedding planes and formation parameters on the fracture height propagation mechanism, a two-dimensional hydraulic fracturing simulation model considering bedding planes is established, as shown in Fig. 5 The model has a width of 60 m in the X-direction and a height of 80 m in the Y-direction, comprising three blocks and two contact surfaces. Tetrahedral elements are used for meshing. Considering both computational accuracy and simulation efficiency, the mesh size in both X and Y directions is set to 2 m, totaling 1200 block elements. In the Y direction, the top and bottom of the model are coal gangue layers with a thickness of 30 m each, and the middle is coal rock layer with a thickness of 20 m. The contact surface between the top coal gangue layer and the coal rock layer is set as the upper layer. The contact surface between the bottom coal gangue layer and the coal rock layer is set as the lower layer, and the spacing between the upper and lower layers is 20 m. During simulation calculations: For the stress field, the minimum horizontal stress σ_h is applied in the X-direction, and the vertical stress σ_v is applied in the Y-direction. The horizontal geostress in the coal parting layer is σ_{h1}, and in the coal rock layer, it is σ_{h2}. For the seepage field, the initial pore pressure of the reservoir is set to 20 MPa. The injection point is located at the center of the model with coordinates (30, 40). Slickwater is selected as the fracturing fluid, injected in constant-rate mode. The simulated pumping duration is 720 s.

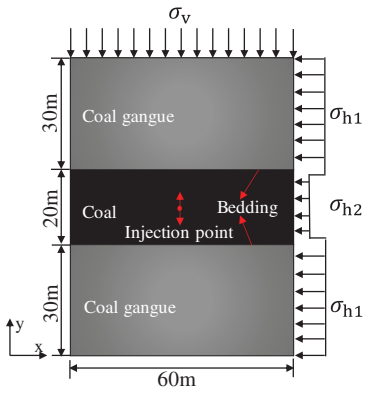

Figure 5: Schematic diagram of a 2D hydraulic fracturing model for deep coal-rock reservoirs

2.3.2 Model Parameter Selection

Geomechanical parameters for the computational model were determined based on actual geological data from the No. 8 coal seam within the Taiyuan Formation along the southeastern margin of the Ordos Basin, with specific values provided in Table 1. Fracturing fluid parameters included an injection rate of 0.003 m^2/s, a viscosity of 2.5 mPa·s, and a density of 1000 kg/m^3.

Table 1: Basic parameters of the model parameters

Parameters	Coal value	Coal Gangue value
Density/kg·m^{-3}	1490	1900
Young's modulus/GPa	5	15
Poisson's ratio	0.35	0.3
Tensile strength/MPa	2.5	4.5
Cohesion/MPa	3	4
Internal friction Angle/°	35	35
Permeability coefficient	1×10^{-14}	1×10^{-14}
Dilatancy angle/°	15	15
Vertical stress/MPa	52	52
Minimum horizontal principal stress/MPa	50	51.5
Bedding plane cohesion/MPa	2	2
Bedding plane internal friction angle/°	30	30
Bedding plane tensile strength/MPa	1	1

2.3.3 Model Correctness Verification

Building upon the theoretical framework of the Penny-shaped model, this study validates the accuracy of the fracture propagation model and grid convergence by comparing numerical solutions with classical analytical solutions. The benchmark model used for verification, depicted in Fig. 6, has dimensions of 30 m × 30 m × 20 m, with a constant-rate injection point located at its geometric center. Detailed parameters are summarized in Table 2.

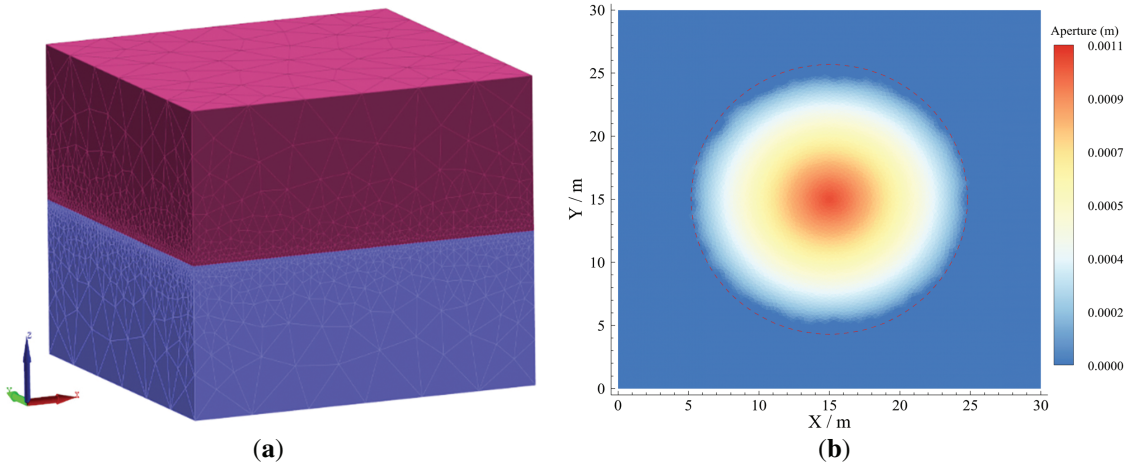

(**a**) (**b**)

Figure 6: Schematic diagram of the validation of the numerical model of CDEM hydraulic fracturing fracture extension: (**a**) Schematic diagram of fracture propagation numerical model validation; (**b**) Numerical simulation results diagram of Penny-shaped fracture

Table 2: Model validation parameters

Parameters	Value
Rock density/kg·m^{-3}	2500
Poisson's ratio	0.2
Internal friction angle/°	40
Water density/kg·m^{-3}	1000
Permeability/mD	100
Fracture toughness/MPa·m$^{0.5}$	2.12
Elastic modulus/GPa	20
Cohesion/MPa	10
Tensile strength/MPa	3
Injection rate/m^3·s^{-1}	0.005
Viscosity/mPa·s	1000

In the Penny-shaped model, the dimensionless toughness parameter κ is defined to differentiate fracture mechanisms: $\kappa < 1$ characterizes viscosity-dominated fractures, while $\kappa > 3.5$ characterizes toughness-dominated fractures (Dontsov, 2016) [28]. The expression for this parameter is given in Eq. (32).

$$\kappa = K' \left(\frac{t^2}{\mu'^5 Q_0^3 E'^{13}} \right)^{\frac{1}{18}} \tag{32}$$

$$K' = 4\sqrt{\frac{2}{\pi}} K_{IC} \tag{33}$$

$$E' = \frac{E}{1-\nu^2}, \mu' = 12\mu \tag{34}$$

where t is the injection time, s. Q_0 is the displacement, m^3/s. K_{IC} is the fracture toughness, MPa·m$^{0.5}$. μ is the fracturing fluid viscosity, Pa·s. E is the Young's modulus, GPa. ν is the Poisson's ratio.

With an injection rate of 0.005 m^3/s, a fluid viscosity of 0.001 Pa·s, and an injection time of 22 s, the value of κ calculated from Eq. (32) is 8.80, which exceeds the threshold value of 3.5. This indicates that the fracture propagation is toughness-dominated. Consequently, the analytical solution for a toughness-dominated Penny-shaped fracture (M-analytical solution) is applied.

A comparison between numerical and analytical solutions is presented in Fig. 7. Specifically, Fig. 7a depicts the evolution of fracture length over time, and Fig. 7b shows the variation of fracture aperture along the radial direction. Throughout the fracture propagation simulation, the average relative error between the numerical and analytical solutions remains within 10% for both fracture length and aperture, indicating strong agreement. These results confirm the accuracy of the fracture propagation model developed in this study.

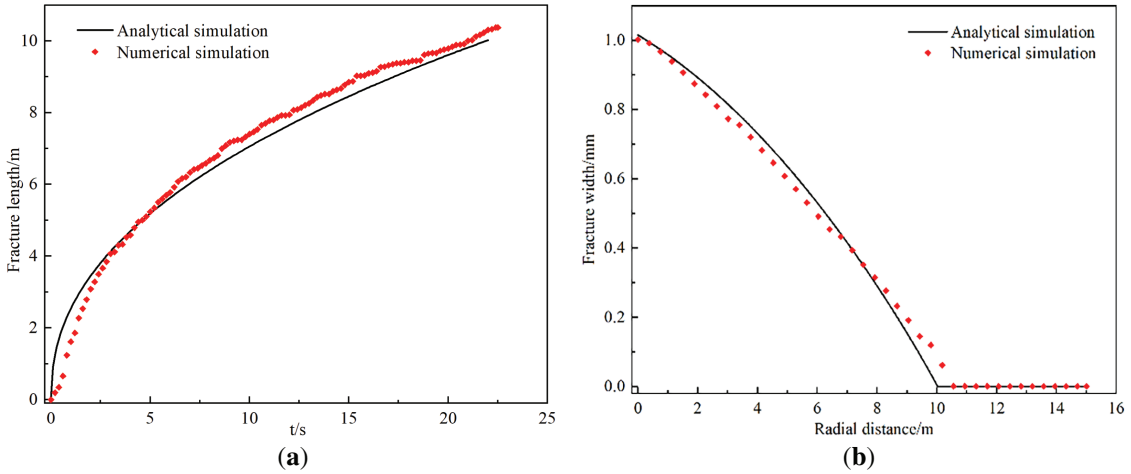

Figure 7: Results comparison diagram of fracture propagation numerical simulation and analytical solutions. (**a**) Fracture length vs. time evolution curve; (**b**) Fracture width vs. radial distance curve

3 Numerical Simulation Results Analysis

3.1 Influence of Vertical Stress Difference

Under constant other parameters with fixed minimum horizontal principal stress, altering only the vertical principal stress examines vertical stress difference's influence on hydraulic fracture vertical propagation in deep coal-rock. Fig. 8 shows simulations for vertical principal stresses of 52, 53, 55, and 57 MPa (corresponding vertical stress differences: 2, 3, 5, 7 MPa). Increasing vertical stress difference drives three fracture propagation stages: fractures captured then diverted along bedding planes, fractures confined within coal-rock reservoirs by bedding plane constraints, and fractures penetrating interlayer interfaces into partings.

As illustrated in Fig. 9a, the fracture width at the central injection point initially increases and subsequently decreases with increasing vertical stress difference. This non-monotonic trend primarily stems from the following mechanisms: when the vertical stress difference is 5 MPa, bedding planes remain unopened, leading to full energy allocation toward enhancing shear displacement. However, a more significant reduction in fracture width occurs after bedding planes are penetrated. When the vertical stress difference ranges from 2 to 5 MPa, hydraulic fractures are captured or terminated by interlayer interfaces without penetrating adjacent strata. Under these conditions, fracture aperture at the injection point exhibits an increasing trend with rising vertical stress difference, reaching a maximum value of 15.66 mm. When the vertical stress difference exceeds 5 MPa, hydraulic fractures penetrate interlayer interfaces and propagate vertically. Concurrently, fracture aperture at the injection point demonstrates a progressive reduction with increasing stress differential. As evidenced in Fig. 9b, an increase in vertical stress difference from 2 to 3 MPa reduces the bedding plane aperture at the central region by 0.57 mm and decreases the fractured zone extent by 43.8%. In cases where hydraulic fractures are terminated by or penetrate through interlayer interfaces, no shear or tensile failure occurs along bedding planes.

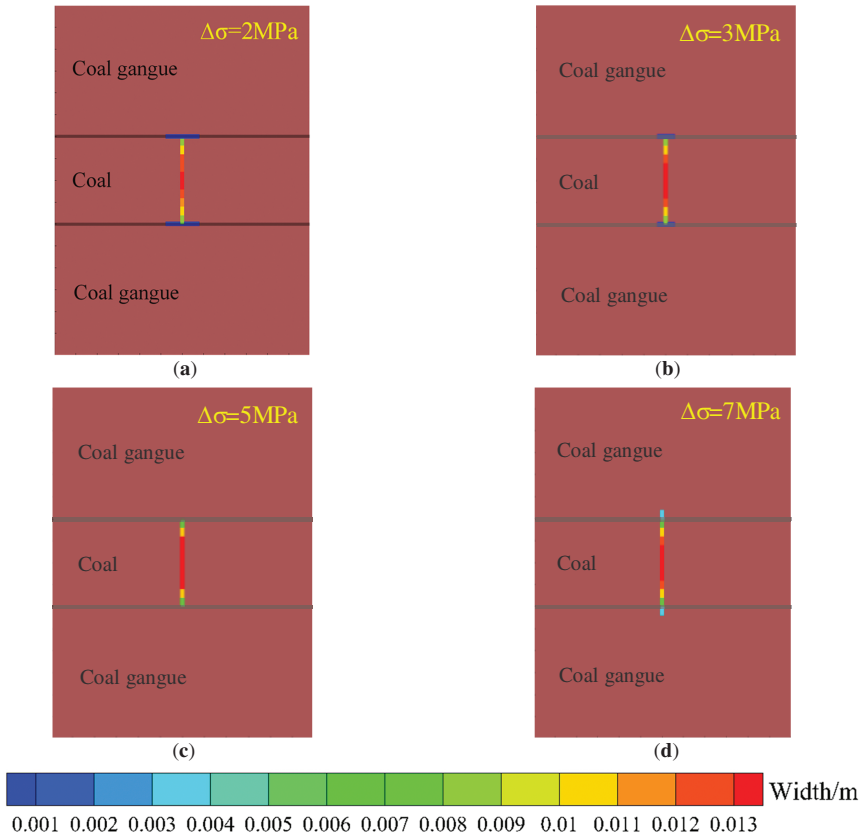

Figure 8: Hydraulic fracture propagation morphology diagrams under different vertical stress differences. (**a**) 2 MPa; (**b**) 3 MPa; (**c**) 5 MPa; (**d**) 7 MPa

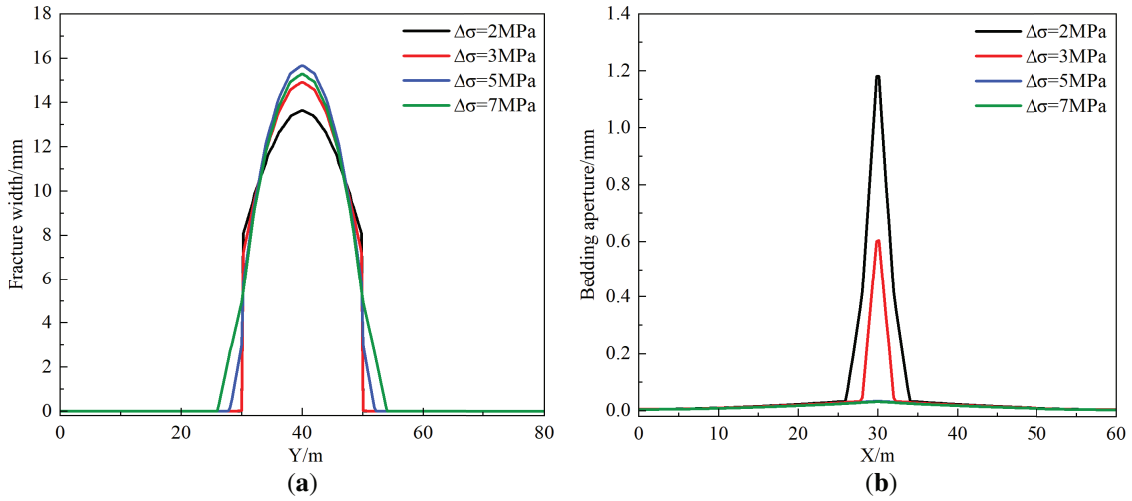

Figure 9: Numerical simulation result curves of hydraulic fracturing under different vertical stress. (**a**) *Y*-direction hydraulic fracture aperture variation curve; (**b**) bedding plane aperture variation curve in *X*-direction

3.2 Influence of Elastic Modulus

With other geological and operational parameters held constant and the elastic modulus of the parting layer fixed at 15 GPa, variations in the coal-rock layer's elastic modulus (5, 10, 20, 25 GPa) investigate the influence of elastic modulus contrast on hydraulic fracture cross-layer propagation. Fig. 10 simulation results indicate: when the elastic modulus E_1 of the coal-rock layer is 1/3, 2/3, 4/3, 5/3 of the parting layer modulus E_2, hydraulic fractures initiating from the coal-rock layer fail to achieve cross-layer propagation, while fracture aperture at the injection point gradually decreases, and bedding activation range progressively expands, demonstrating that elastic modulus contrast inhibits fracture penetration while enhancing bedding activation effects.

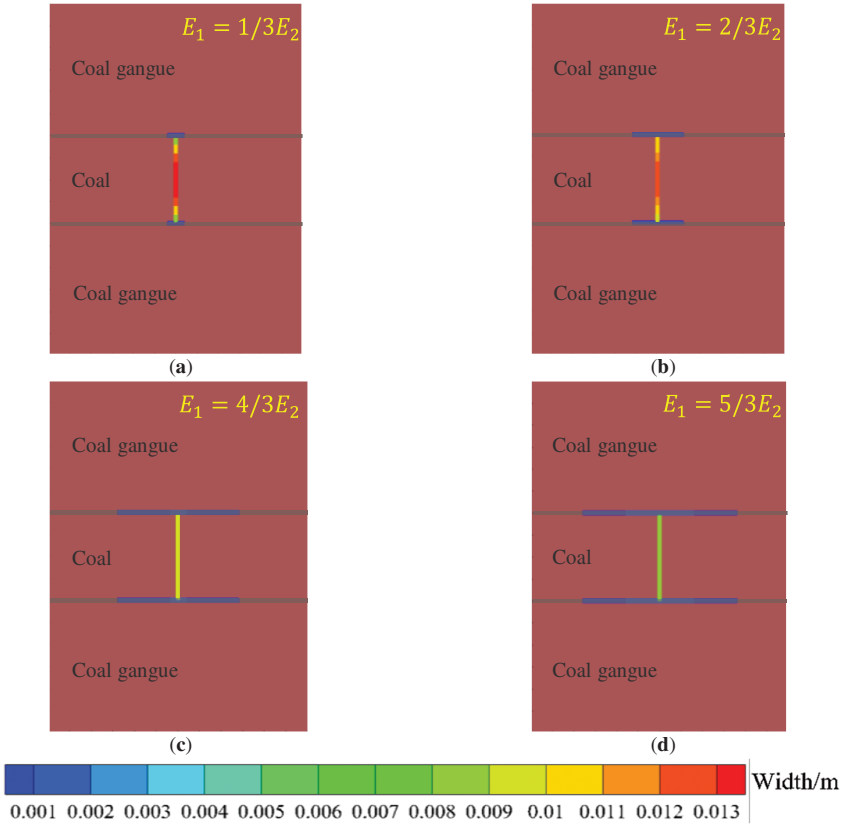

Figure 10: Hydraulic fracture propagation morphology diagram under different formation elastic moduli. (**a**) 5 MPa; (**b**) 10 MPa; (**c**) 20 MPa; (**d**) 25 MPa

Fig. 11 shows that as the coal-rock reservoir elastic modulus increases, hydraulic fractures propagate faster vertically, reaching bedding planes quicker, significantly increasing bedding aperture and activation range, whereas injection-point aperture declines. Increasing coal-rock elastic modulus from 5 to 25 GPa reduces fracture aperture by 42.6%, elevates bedding aperture by 0.86 mm, and expands bedding activation range by 31.9 m. Mechanistically, lower elastic modulus indicates higher rock plasticity, increasing fracture width within coal-rock, suppressing fracture-tip stress concentration effects, thereby decelerating propagation rates and reducing bedding activation degree.

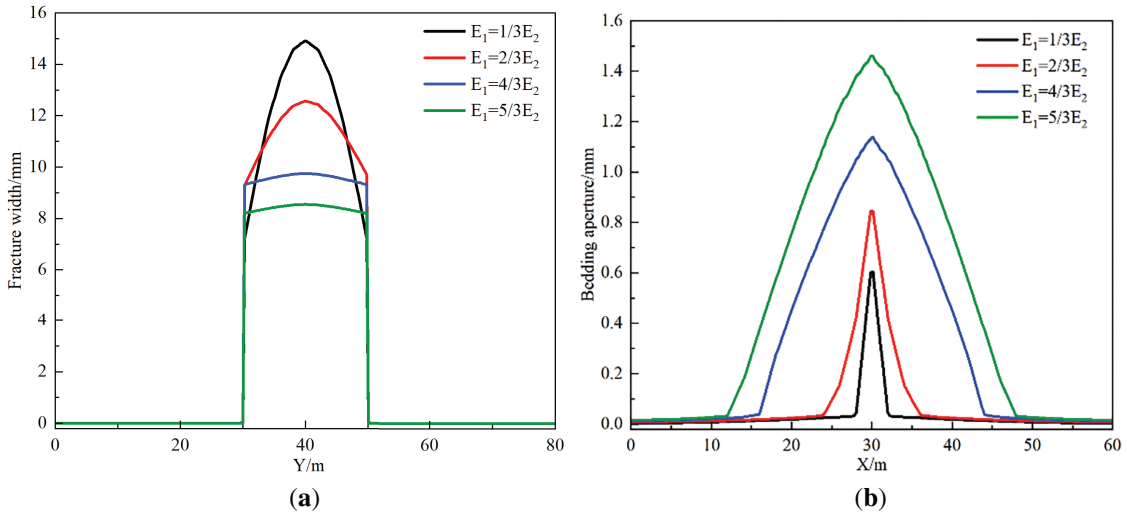

Figure 11: Hydraulic fracturing numerical simulation result curves under different elastic moduli. (**a**) *Y*-direction hydraulic fracture aperture variation curve; (**b**) bedding plane aperture variation curve in *X*-direction

3.3 Influence of Bedding Plane Cohesion

Bedding plane cohesion (c) is the key mechanical parameter controlling hydraulic fracture penetration through layers, therefore this section investigates the influence of bedding plane cohesion on fracture propagation in the height direction. Keeping other geological and operational parameters unchanged, bedding plane cohesion is varied to 2.5, 3.5, 4.5, and 5.5 MPa, with fracture morphology results shown in Fig. 12.

Fig. 12 displays hydraulic fracture propagation morphologies under different bedding plane cohesion values. When cohesion is below 3.5 MPa, hydraulic fractures are captured or terminated by bedding planes; when cohesion exceeds 4.5 MPa, fractures penetrate bedding planes and propagate into adjacent layers. As illustrated in Fig. 13, as bedding plane cohesion increases from 2.5 to 3.5 MPa, fracture width at the injection point increases by 0.95 mm; when cohesion further rises to 4.5 MPa, hydraulic fractures penetrate bedding planes, and fracture width at the injection point decreases by 0.52 mm. At 2.5 MPa cohesion, bedding aperture measures 0.61 mm with an activation range of 4.54 m. Research results indicate: when bedding plane cohesion is low, its interfacial strength is significantly lower than the energy required to overcome interlayer stress differences and rock tensile strength, causing fracture tips to preferentially propagate along paths of lower energy consumption, thereby inhibiting cross-layer propagation; when bedding plane cohesion is high, hydraulic fractures generate sufficient net pressure at their tips under high driving forces, enabling penetration through bedding planes. Bedding plane cohesion exerts significant control over hydraulic fracture penetration behavior but has minimal impact on dynamic width variations at the injection point.

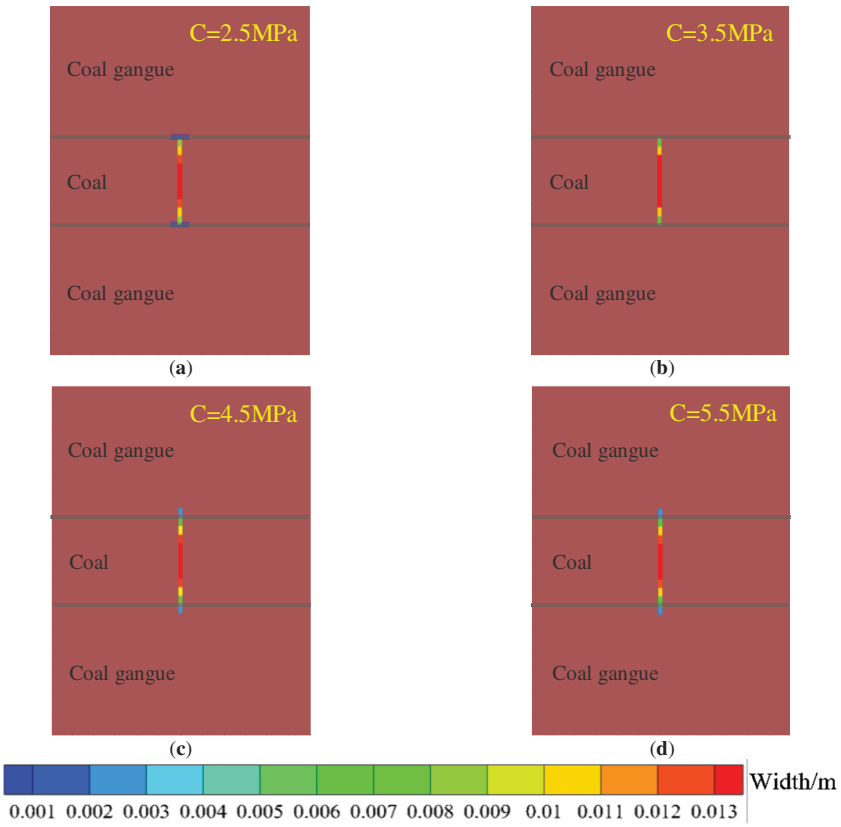

Figure 12: Hydraulic fracture propagation morphology diagram under different bedding plane cohesion. (**a**) 2.5 MPa; (**b**) 3.5 MPa; (**c**) 4.5 MPa; (**d**) 5.5 MPa

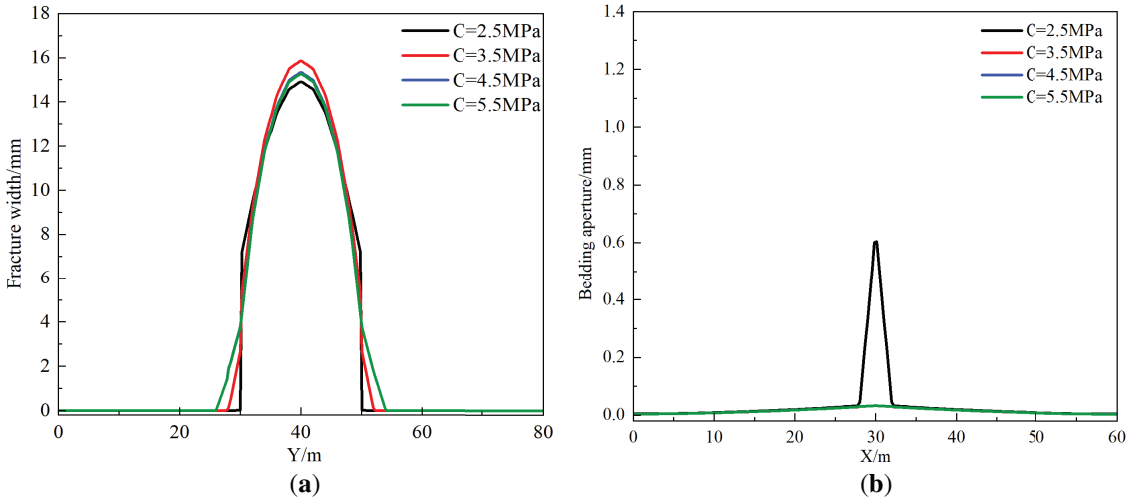

Figure 13: Hydraulic fracturing numerical simulation result curves under different bedding plane cohesion. (**a**) *Y*-direction hydraulic fracture aperture variation curve; (**b**) bedding plane aperture variation curve in *X*-direction

3.4 Influence of Interlayer Stress Difference

The interlayer stress difference ($\Delta\sigma_h = \Delta\sigma_{h1} - \Delta\sigma_{h2}$) is one of the key factors controlling hydraulic fracture propagation in the vertical direction. Keeping other geological and operational parameters unchanged, the minimum horizontal principal stress of the coal seam ($\Delta\sigma_{h2}$) is fixed at 50 MPa, while the minimum horizontal principal stress of the parting layer ($\Delta\sigma_{h1}$) is varied to 50, 51.5, 53, and 54.5 MPa. This setup studies the influence of different interlayer stress differences (0, 1.5, 3, 4.5 MPa) on hydraulic fracture penetration through layers, with fracture morphology results shown in Fig. 14.

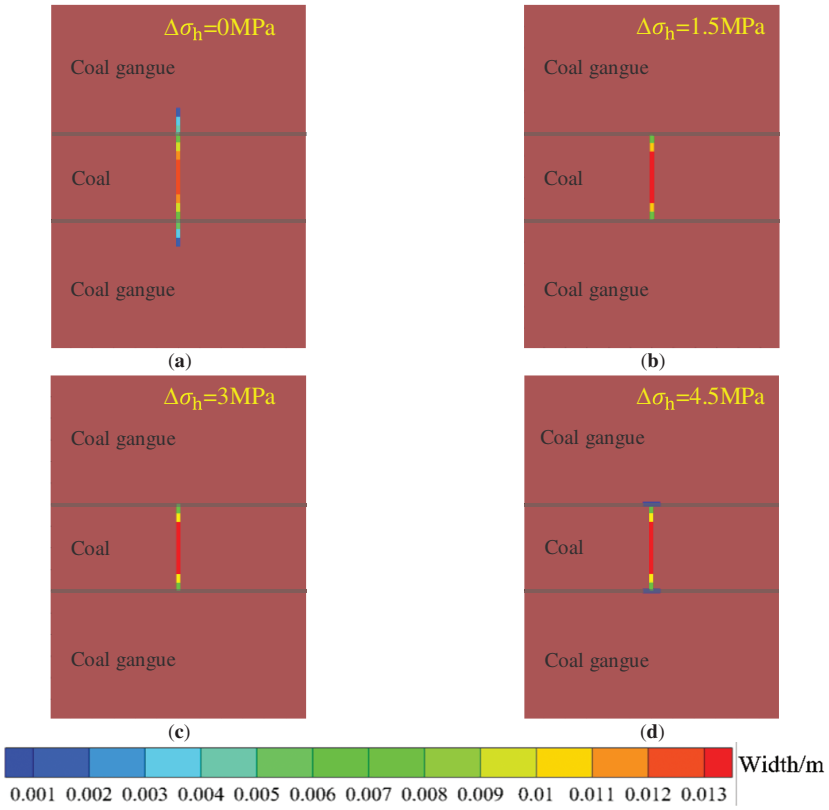

Figure 14: Fracture width distribution under different interlayer stress difference. (**a**) 0 MPa; (**b**) 1.5 MPa; (**c**) 3 MPa; (**d**) 4.5 MPa

Fig. 14 displays hydraulic fracture propagation morphologies under different interlayer stress differences. As the interlayer stress difference increases, hydraulic fracture behavior exhibits staged evolution: transitioning from initial penetration through layers to gradual suppression by bedding planes, and finally being fully captured by the bedding interface, deflecting to propagate along the bedding direction. As shown in Fig. 15, when the interfacial stress difference increases from 0 to 3 MPa, the fracture width at the injection point increases from 13.04 to 15.78 mm, representing an increase of approximately 21%. Additionally, at an interlayer stress difference of 4.5 MPa, the bedding plane opens, with a central aperture of 0.28 mm and an activation range of 5.21 m. When the interlayer stress difference exceeds 1.5 MPa, as the fracture tip approaches the high-stress barrier layer, the stress barrier formed by the high-stress zone increases the energy required for continued vertical propagation, causing the fracture tip to deflect and preferentially propagate along the bedding plane weak interfaces.

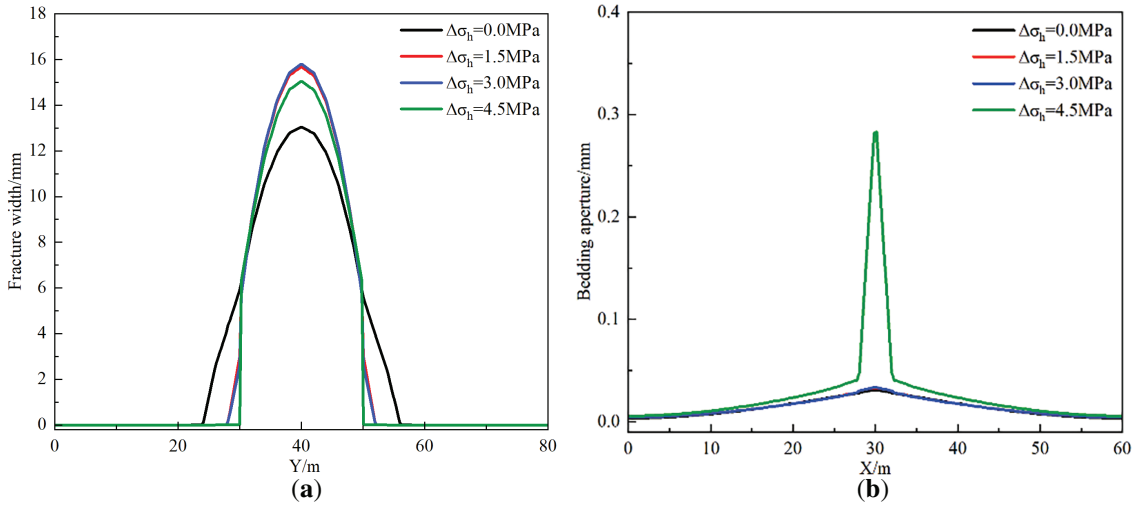

Figure 15: Hydraulic fracturing numerical simulation result curves under different interlayer stress difference. (**a**) *Y*-direction hydraulic fracture aperture variation curve; (**b**) bedding plane aperture variation curve in *X*-direction

3.5 Influence of Fracturing Fluid Flow Rate

During hydraulic fracturing operations, different fracturing fluid flow rates provide varying net pressures for fracture propagation, which critically determines whether hydraulic fractures can penetrate through bedding planes. Therefore, while keeping other geological parameters constant, numerical simulations were conducted for flow rates of 0.003, 0.006, 0.009, and 0.012 m^2/s, with results illustrated in Fig. 16. The simulations demonstrate that as the flow rate increases, hydraulic fractures transition from being captured by bedding planes to penetrating through them, subsequently propagating perpendicular to the minimum horizontal principal stress direction.

As shown in Fig. 17, the fracture width at the injection point and bedding aperture were extracted to quantitatively analyze the effect of flow rate on fracture penetration. Higher injection rates significantly increase net pressure within the fracture, enabling the fracture tip to overcome bedding plane barriers and penetrate through layers. When the flow rate exceeds 0.006 m^2/s, fractures consistently penetrate the coal-parting interface, with earlier penetration timing and sustained height growth at higher rates. Increasing the flow rate from 0.003 to 0.012 m^2/s enlarges the fracture width at the injection point by 8.38 mm (a 56.2% increase), attributed to greater fluid energy widening the fracture. Additionally, bedding planes only opened at the lowest rate (0.003 m^2/s), exhibiting a central aperture of 0.60 mm and an activation range of 4.66 m. Overall, higher flow rates reduce height containment, significantly elevating the risk of height breakthrough into non-target layers. Consequently, flow rate optimization is essential for effective stimulation of composite reservoirs.

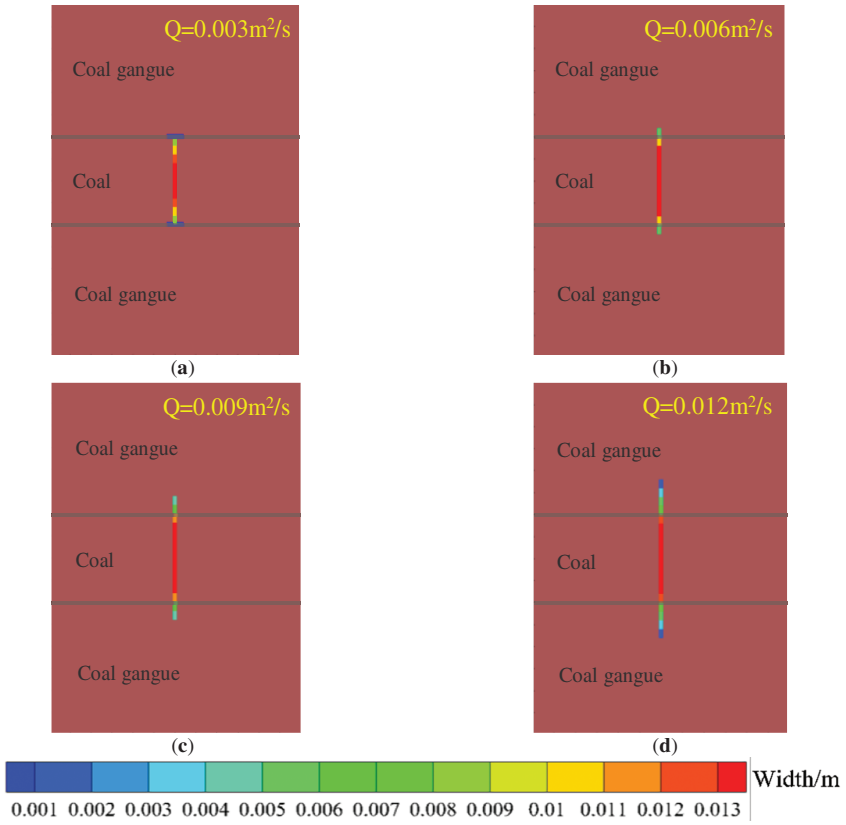

Figure 16: Hydraulic fracture morphology under varying fracturing fluid flow rate. (**a**) 0.003 m^2/s; (**b**) 0.006 m^2/s; (**c**) 0.009 m^2/s; (**d**) 0.012 m^2/s

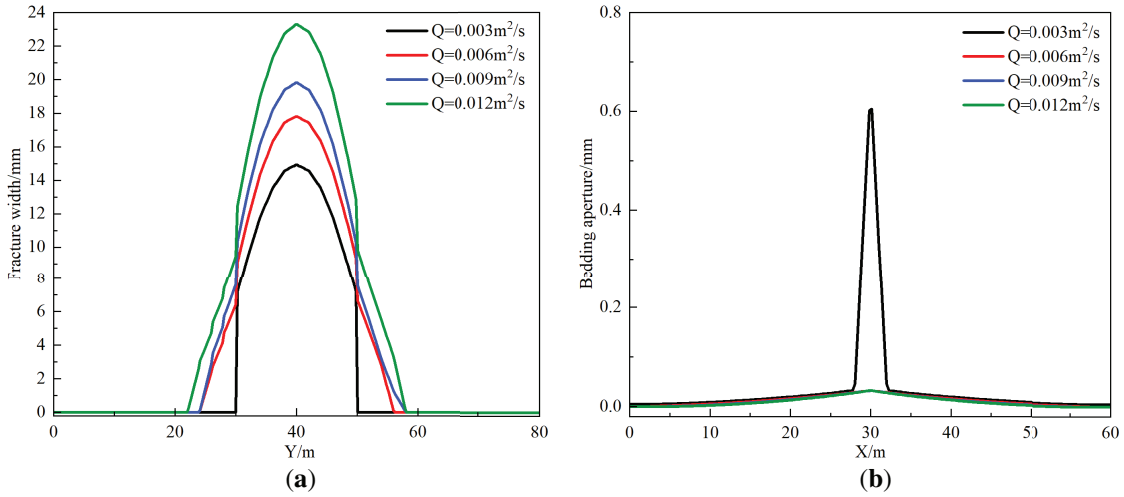

Figure 17: Hydraulic fracturing numerical simulation result curves under different fracturing fluid flow rate. (**a**) *Y*-direction hydraulic fracture aperture variation curve; (**b**) bedding plane aperture variation curve in *X*-direction

4 Conclusion

This study utilizes the Combined Continuous-Discontinuous Element Method (CDEM) to develop a numerical model simulating hydraulic fracture propagation in deep coal seams containing interbedded partings. Using this framework, a controlled-variable methodology was employed to systematically evaluate the effects of key parameters—such as vertical stress difference, elastic modulus, interfacial cohesion, interlayer stress contrast, and injection rate—on fracture penetration behavior across coal-parting interfaces. The main results are concluded as follows:

1. In the deep coal rock with weak plane structure, the propagation behavior of hydraulic fracture mainly presents three stages of change: the fracture is captured by the bedding plane and then turns to propagate along the bedding plane; the fracture propagation is limited by the bedding plane in the coal rock reservoir; the fracture breaks through the interlayer interface and propagates in the gangue layer.
2. Under deep coal reservoir conditions, elevated vertical stress differences and enhanced bedding cohesion facilitate hydraulic fracture penetration through bedding planes, promoting propagation within parting interlayers. During cross-layer fracturing events, bedding planes remain intact without shear or tensile failure, while a discernible reduction in fracture aperture is observed at the injection point.
3. An increased contrast in elastic modulus between coal and gangue inhibits the penetration of hydraulic fractures across the interfacial boundary. The greater modulus difference promotes more extensive activation of bedding planes, thereby enhancing the stimulation effectiveness of the coalbed methane reservoir.
4. Elevated interlayer stress contrast establishes a stress barrier that impedes hydraulic fracture penetration across bedding interfaces. Compared to scenarios lacking interlayer stress differentials, this configuration yields an approximately 21% increase in fracture aperture at the injection point.
5. Higher fracturing fluid injection rates promote hydraulic fracture penetration across coal-parting interfaces, significantly reducing the time required for cross-layer propagation. Elevated injection rates further drive progressive expansion of fracture aperture and height post-penetration. For effective stimulation of composite reservoirs, injection rate optimization must align with specific engineering objectives.

Acknowledgement: The authors gratefully acknowledge the invaluable support provided by the Research Institute of Petroleum Engineering Technology, SINOPEC Jiangsu Oilfield Company.

Funding Statement: The authors received no specific funding for this study.

Author Contributions: The authors confirm their contributions to the paper as follows: Study conception and design: Zhirong Jin, Xiaorui Hou; Data collection: Yanrong Ge; Analysis and interpretation of results: Tiankui Guo, Ming Chen; Draft manuscript preparation: Shuyi Li, Tianyu Niu. All authors reviewed the results and approved the final version of the manuscript.

Availability of Data and Materials: The dataset generated and analyzed during the current study is available from the corresponding author upon reasonable request.

Ethics Approval: Not applicable.

Conflicts of Interest: The authors declare no competing financial interests or personal relationships that could have appeared to influence the work reported in this paper.

References

1. Jiang SH, Shi SZ, Zhao K, Liu YC, Yao XJ, Shi JX, et al. Prospect and development direction of deep coal and coalbed methane exploration. Sci Technol Rev. 2023;41:106–13. (In Chinese).

2. Kang Y, Huangfu Y, Zhang B, He Z, Jiang S, Ma YZ. Gas oversaturation in deep coals and its implications for coal bed methane development: a case study in Linxing Block, Ordos Basin, China. Front Earth Sci. 2023;10:1031493. doi:10.3389/feart.2022.1031493.
3. An Y, Sun Z, Wang J, Zhang X, Sun Y. Numerical simulation of deep coalbed methane development based on embedded discrete fracture model: a triple medium flow approach. Energy Sci Eng. 2025;13(6):3045–62. doi:10.1002/ese3.70085.
4. Wan Y, Wang Z, Hu D, Wang Y, Huo M, Mu X, et al. Gas-bearing evaluation of deep coal rock in the Yan'an gas field of the Ordos Basin. Front Earth Sci. 2024;12:1438834. doi:10.3389/feart.2024.1438834.
5. Feng R, Li C, Sun L, Wang J, Liu J, Li N. Study on the influence of deep coalbed methane horizontal well deployment orientation on production. Energies. 2024;17(22):5784. doi:10.3390/en17225784.
6. Guo F, Lv R, Song D, Li Y, Zhang Z, Wang X, et al. Coalbed methane enhancement in low-permeability reservoirs by hydraulic fracturing with coated ceramsite. Energy Fuels. 2023;37(13):9023–31. doi:10.1021/acs.energyfuels.3c00496.
7. Xiong D, He J, Ma X, Qu Z, Guo T, Ma S. Fracturing simulation with different perforation positions at deep coal seam and roof/floor rock—case study at the No. 8 deep coal seam of a gas field in the Ordos Basin. J China Coal Soc. 2024;49(12). (In Chinese). doi:10.13225/j.cnki.jccs.2024.0009.
8. Cao S, Wang X, Ge Z, Zhang L, Yang Y, Hu H. Dynamic damage mechanism of coal with high true triaxial stress level subject to water jets. Powder Technol. 2024;437(8):119583. doi:10.1016/j.powtec.2024.119583.
9. Chen B, Barboza BR, Sun Y, Bai J, Thomas HR, Dutko M, et al. A review of hydraulic fracturing simulation. Arch Comput Meth Eng. 2022;29(4):1–58. doi:10.1007/s11831-021-09653-z.
10. Wang C, Li S, Liu L, Liu L. Research on hydraulic fracturing technology of long boreholes along strata of high vast thick coal seam. Adv Civ Eng. 2024;2024(1):6305640. doi:10.1155/2024/6305640.
11. Sun Z, Tan Z, Lin J, An Q, Zou Y, Liu S, et al. Investigation into hydraulic fracture propagation behavior during temporary plugging and diverting fracturing in deep coal seam. Front Energy Res. 2024;12:1369428. doi:10.3389/fenrg.2024.1369428.
12. Shi Y, He Y, Wan J, Sun J, Zeng J, Cui R. The primary controlling factors of the occurrence state of deep high-rank coalbed methane in eastern Ordos Basin. Front Earth Sci. 2024;12:1340523. doi:10.3389/feart.2024.1340523.
13. Daneshy AA. Hydraulic fracture propagation in layered formations. Soc Petrol Eng J. 1978;18(1):33–41. doi:10.2118/6088-pa.
14. Zhao H, Chen M. Extending behavior of hydraulic fracture when reaching formation interface. J Petrol Sci Eng. 2010;74(1–2):26–30. doi:10.1016/j.petrol.2010.08.003.
15. Tan P, Jin Y, Han K, Zheng X, Hou B, Gao J, et al. Vertical propagation behavior of hydraulic fractures in coal measure strata based on true triaxial experiment. J Petrol Sci Eng. 2017;158(6):398–407. doi:10.1016/j.petrol.2017.08.076.
16. Tian Z, Xiong Z, Wei Y, Ma S, Hu X. Numerical simulation of fracture propagation in deep coal seam reservoirs. Energy Sci Eng. 2023;11(10):3559–74. doi:10.1002/ese3.1540.
17. Ren Q, Zhao Y, Zhu X, Zhou Y, Jiang Y, Wang P, et al. CDEM-based simulation of the 3D propagation of hydraulic fractures in heterogeneous Coalbed Methane reservoirs. Comput Geotech. 2022;152(4):104992. doi:10.1016/j.compgeo.2022.104992.
18. Xu W, Zhao J, Rahman SS, Li Y, Yuan Y. A comprehensive model of a hydraulic fracture interacting with a natural fracture: analytical and numerical solution. Rock Mech Rock Eng. 2019;52(4):1095–113. doi:10.1007/s00603-018-1608-9.
19. Huang L, Li B, Wang B, Zhang J. Effects of coal bedding dip angle on hydraulic fracturing crack propagation. Geomech Geophys Geo Energy Geo Resour. 2023;9(1):30. doi:10.1007/s40948-023-00562-y.
20. Zhu X, Feng C, Cheng P, Wang X, Li S. A novel three-dimensional hydraulic fracturing model based on continuum-discontinuum element method. Comput Meth Appl Mech Eng. 2021;383(6):113887. doi:10.1016/j.cma.2021.113887.
21. Zhang B, Guo T, Chen M, Wang J, Cao J, Wang H, et al. Effect of bedding planes and property contrast between layers on the propagation mechanism of hydraulic fracture height in shale reservoirs. Comput Geotech. 2024;175(12):106715. doi:10.1016/j.compgeo.2024.106715.

22. Li J, Wang L, Feng C, Zhang R, Zhu X, Zhang Y. Study on the influence of perforation parameters on hydraulic fracture initiation and propagation based on CDEM. Comput Geotech. 2024;167(3):106061. doi:10.1016/j.compgeo.2023.106061.
23. Zhang B, Guo T, Chen M, Wang J, Qu Z, Wang H, et al. Research on fracture propagation of hydraulic fracturing in a fractured shale reservoir using a novel CDEM-based coupled HM model. Comput Geotech. 2024;168(3):106170. doi:10.1016/j.compgeo.2024.106170.
24. Xu Z, Zhao H, Liu X, Liang L, Luo P. Three-dimensional numerical simulation of fracture extension in conglomerate fracturing considering pore-fracture seepage and study of influencing factors. Geofluids. 2024;2024(1):7883958. doi:10.1155/2024/7883958.
25. Lu Y, Cai Z, Huang D, Yao X, Ma Q, Chen D. Peridynamic modeling and analysis of interfacial crack propagation by hydraulic fracturing in layered shale. Comput Geotech. 2025;184(16):107280. doi:10.1016/j.compgeo.2025.107280.
26. Hwang J, Manchanda R, Sharma MM. An extended finite volume model for implicit cohesive zone fracture propagation in a poroelastic medium. Comput Meth Appl Mech Eng. 2019;350:571–94. doi:10.1016/j.cma.2019.03.040.
27. Wang J, Guo T, Chen M, Qu Z, Zhang B, Zhang W, et al. Numerical simulation of fracture propagation morphology in hydraulic fracturing development of geothermal reservoirs based on the CDEM-THM3D. Comput Geotech. 2024;172(05):106444. doi:10.1016/j.compgeo.2024.106444.
28. Dontsov EV. An approximate solution for a penny-shaped hydraulic fracture that accounts for fracture toughness, fluid viscosity and leak-off. R Soc Open Sci. 2016;3(12):160737. doi:10.1098/rsos.160737.